J. Fluid Mech. (2001), *vol.* 443, *pp.* 301–328. Printed in the United Kingdom

Finite-amplitude solitary states in viscoelastic shear flow: computation and mechanism

By K. ARUN KUMAR AND MICHAEL D. GRAHAM†

Department of Chemical Engineering and Rheology Research Center,
University of Wisconsin-Madison, Madison, WI 53706-1691, USA

(Received 1 August 2000 and in revised form 11 April 2001)

Starting from stationary bifurcations in Couette–Dean flow, we compute stationary nontrivial solutions in the circular Couette geometry for an inertialess finitely extensible nonlinear elastic (FENE-P) dumbbell fluid. These solutions are isolated from the Couette flow branch arising at finite amplitude in saddle–node bifurcations as the Weissenberg number increases. Spatially, they are strongly localized axisymmetric vortex pairs embedded in an arbitrarily long 'far field' of pure Couette flow, and are thus qualitatively, and to some extent quantitatively, similar to the 'diwhirl' (Groisman & Steinberg 1997) and 'flame' patterns (Baumert & Muller 1999) observed experimentally. For computationally accessible parameter values, these solutions appear only above the linear instability limit of the Couette base flow, in contrast to the experimental observations. Correspondingly, they are themselves linearly unstable. Nevertheless, extrapolation of the trend in the bifurcation points with increasing polymer extensibility suggests that for sufficiently high extensibility the diwhirls will come into existence before the linear instability, as seen experimentally.

Based on the computed stress and velocity fields, we propose a fully nonlinear self-sustaining mechanism for these flows. The mechanism is related to that for viscoelastic Dean flow vortices and arises from a finite-amplitude perturbation giving rise to a locally unstable profile of the azimuthal normal stress near the outer cylinder at the symmetry plane of the vortex pair. The unstable stress profile, in combination with a 'tubeless siphon' effect, nonlinearly sustains the patterns. We propose that these solitary, strongly nonlinear structures comprise fundamental building blocks for complex spatiotemporal dynamics in the flow of elastic liquids.

1. Introduction

Spatially localized structures are common in pattern-forming physical systems (Cross & Hohenberg 1993). Such patterns are interesting and important because they are an indication of significant nonlinear effects, and their interaction with other patterns may give information on spatiotemporal behaviour. Examples of oscillatory localized structures can be found in binary liquid mixtures (Moses, Fineberg & Steinberg 1987; Heinrichs, Ahlers & Cannell 1987; Kolodner, Bensimon & Surko 1988), parametrically excited surface waves (Wu, Keolian & Rudnick 1984), elastic media (Wu *et al.* 1987), granular media (Umbanhowar, Melo & Swinney 1996; Lioubashevski, Arbell & Fineberg 1996; Fineberg & Lioubashevski 1998), and colloidal suspensions (Lioubashevski *et al.* 1999). Recently, stationary, two-dimensional finite-amplitude localized states have been computed in Newtonian plane Couette

† Author to whom correspondence should be addressed: e-mail: graham@engr.wisc.edu

flow (Cherhabili & Ehrenstein 1995, 1997). These solutions are isolated from the base Couette flow branch and were computed by numerical continuation of travelling wave solutions in plane Poiseuille flow. Although unstable, these may be related to coherent structures observed in turbulent plane Couette flow.

In flows of viscoelastic liquids, long-wavelength structures were first observed by Beavers & Joseph (1974) in a circular Couette device. These structures, termed 'tall Taylor cells', are primarily inertia-driven patterns (Taylor vortices) modified by elasticity. Similar patterns have been computed by Lange & Eckhardt (2001)†. Recently, long-wavelength, stationary, axisymmetric vortex pair structures have been observed in inertialess viscoelastic circular Couette flow by Groisman & Steinberg (1997, 1998) and Baumert & Muller (1999). There are three interesting aspects to these observations: (i) isothermal linear stability analysis in this geometry never predicts stationary bifurcations, (ii) these vortex pairs, dubbed 'diwhirls' by Groisman & Steinberg (1997) and 'flame patterns' by Baumert & Muller (1999) are very localized, i.e. there does not seem to be a selected axial wavelength for these patterns, and (iii) the transition back to the base Couette flow is hysteretic, i.e. the shear rate at which the Couette flow base state is recovered is much lower than the onset point at which it loses stability. In the present study, we seek answers to the following questions, motivated by these observations: (i) Do isolated branches of stationary solutions exist in a simple model for a viscoelastic fluid? (ii) Are such solutions, if they exist, localized in space? (iii) Can the results from the computations be used to postulate a self-sustaining mechanism for these structures?

We address these questions by fully nonlinear computations of the branching behaviour of an isothermal inertialess finitely extensible nonlinear elastic (FENE) dumbbell fluid in the circular Couette geometry. Our computations show that an isolated branch of stationary solutions does indeed exist in the circular Couette geometry. In common with the experimentally observed diwhirls, these are long-wavelength solutions that exhibit significant asymmetry between radial inflow and outflow and show hysteresis in Weissenberg number. In addition, these solutions persist at arbitrarily large wavelengths: some of the solutions we have computed have an axial wavelength that is more than a hundred times larger than the gap width. We also use the results from our computations to propose a self-sustaining mechanism for these patterns. Along with the circular Couette flow base state, these structures may form the building blocks for complex spatiotemporal dynamics in the flow of elastic liquids, such as the recently observed phenomenon of elastic turbulence (Groisman & Steinberg 2000). In addition, they may be linked to localized defects seen in polymer processing operations and possibly to the strongly nonlinear and long-wave features observed in free surface flows (Grillet, Lee & Shaqfeh 1999).

Elastic instabilities are common in flows with curved streamlines (Shaqfeh 1996; McKinley, Pakdel & Öztekin 1996). A purely elastic (i.e. zero Reynolds number) instability in circular Couette flow was first observed by Larson, Shaqfeh & Muller (1990), who also elucidated a mechanism for linear instability with respect to time-dependent axisymmetric disturbances. Later computational work (Joo & Shaqfeh 1994; Sureshkumar, Beris & Avgousti 1994) showed that time-dependent non-axisymmetric modes were the most destabilizing, and Joo & Shaqfeh (1994) ex-

† Although these authors denote the solutions that they find as 'diwhirls', their investigation is confined to regimes where $Re \gg 1$ and $We_\theta/Re \ll 1$, where Re and We_θ are Reynolds and Weissenberg numbers respectively. In these parameter regimes, fluid inertia plays a significant role. Thus, the patterns they simulate cannot be classified as being driven by elasticity alone.

panded the mechanism proposed by Larson *et al.* (1990) to include non-axisymmetric modes. Generically, the mechanism for instability in elastic flows is the inward radial force associated with tensile stresses along curved streamlines. Another instability involving non-isothermal effects has been found recently (Al-Mubayedh, Sureshkumar & Khomami 1999); this results in a stationary axisymmetric bifurcation but at shear rates an order of magnitude smaller than where the diwhirls are observed. Therefore, this mechanism appears to have limited relevance for the diwhirls, but seems to explain the very weak stationary vortices seen experimentally by Baumert & Muller (1995, 1997). Hereafter we consider isothermal flow.

The absence of a stationary bifurcation from the circular Couette flow base state means that any branch of stationary solutions that exists in this flow geometry must be isolated from the base state flow, i.e. there can be no direct path from the base state flow to this branch of solutions. One way of accessing such an isolated branch is to introduce an additional parameter that is zero in the limit of circular Couette flow, but for some non-zero value of which there is a stationary bifurcation from the base state. We can find clues to possible parameters that satisfy this criterion by examining flows closely related to viscoelastic circular Couette flow, but where the primary instability is stationary and axisymmetric. One such flow is viscoelastic Dean flow, pressure-driven flow in a curved channel. Experimentally, an approximation to Dean flow may be generated by placing a small obstruction spanning the gap between the two cylinders in a concentric cylinder geometry and then rotating both cylinders at the same angular velocity (Joo & Shaqfeh 1994).

The mechanism of instability in Dean flow, elucidated by Joo & Shaqfeh (1992), is related to the unstable stratification of hoop stress away from the centreline of the channel between the cylinders: this stratification is absent in circular Couette flow. Polymer molecules are more highly stretched outward from the channel centreline. This variation in elastic stresses leads fluid elements to be under radial compression and ultimately to a buckling process leading to the formation of steady axisymmetric vortices. Starting from Dean flow, circular Couette flow can be approached in a smooth way by progressively decreasing the pressure drop, while simultaneously increasing the rotation speed of one of the cylinders. The intermediate flow, where both an azimuthal pressure drop and the cylinder rotation are present as driving forces, is known as Couette–Dean flow. The linear stability characteristics of viscoelastic Couette–Dean flow were studied by Joo & Shaqfeh (1992). As we might expect, this flow is unstable to a stationary axisymmetric mode when the pressure gradient is the dominant driving force, whereas a non-axisymmetric oscillatory mode is the most dangerous when cylinder rotation dominates.

Work on nonlinear analysis in circular Couette and Dean flow has concentrated on regimes close to the bifurcation point – there have been no extensive computational studies of fully nonlinear behaviour in these flows. Renardy *et al.* (1996) conducted a nonlinear analysis to study mode interactions arising from the introduction of inertia into the system. Graham (1998) performed a weakly nonlinear analysis to determine the criticality of the bifurcation in circular Couette flow in the narrow gap limit upon addition of axial flow. Later, Ramanan, Kumar & Graham (1999) extended this analysis to Dean flow. Khayat (1999) used a low-dimensional model in an attempt to determine the dynamical behaviour in purely elastic and inertioelastic circular Couette flow. It should be noted, however, that stress localization (a striking example of which will be seen below) is common in viscoelastic flows, and it is questionable whether such a simple low-dimensional model, which is essentially a low-resolution Galerkin projection, can adequately capture such behaviour.

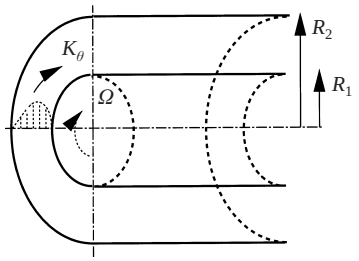

FIGURE 1. Geometry of Couette–Dean flow in an annulus.

The strategy we adopt to search for isolated branches of stationary solutions in circular Couette flow is a fully nonlinear analysis of the governing equations. We use a numerical continuation procedure (Seydel 1994) to trace out stationary non-trivial solutions bifurcating from the trivial branch in Dean or Couette–Dean flow and see if these solutions persist as a parameter is varied smoothly to change the flow from Dean or Couette–Dean to pure circular Couette flow. Any such stationary solutions that persist in the limit of circular Couette flow have to be part of an isolated branch since there is no stationary bifurcation from the base state circular Couette flow. In the remainder of the paper, we report our procedure and results as follows. Section 2 contains a discussion of the geometry, governing equations, and scalings that are used in the computations. In § 3, we present a discussion of the discretization scheme and the numerical method that we use to solve the sparse linear systems arising in the Newton iterations during the continuation process. This section includes discussion on a preconditioner that we have found to be especially useful. In § 4, we discuss the results of continuation in the various parameters, the mechanism of the diwhirl solutions we compute, their stability with respect to axisymmetric and non-axisymmetric oscillatory disturbances, and we present a quantitative comparison of our computed diwhirls with experimental data (Groisman & Steinberg 1998). We also present some results on nonlinear behaviour in Dean flow, where we find that localized patterns do not exist. Finally, we conclude in § 5 with a summary of our main findings.

2. Formulation

We consider the flow of an inertialess polymer solution between two concentric cylinders (figure 1). The inner cylinder has radius R_1 and the outer cylinder has radius R_2. The fluid has a relaxation time λ; the polymer and solvent contributions to the viscosity are denoted respectively by η_p and η_s, with the ratio η_s/η_p denoted by S. The solution viscosity η_t is given by the sum of the solvent and polymer viscosities, $\eta_s + \eta_p$. The flow is created by a combination of the motion of the inner cylinder at a velocity ΩR_1 and by the application of an azimuthal pressure gradient $K_\theta = \partial p/\partial\theta$.

The equations governing the flow are the dimensionless momentum and continuity equations

$$\nabla \cdot \boldsymbol{\tau} - \nabla p + We_\theta S \nabla^2 \boldsymbol{v} = 0, \tag{2.1}$$

$$\nabla \cdot \boldsymbol{v} = 0, \tag{2.2}$$

where $\boldsymbol{v}$ is the velocity, p is the pressure and $\boldsymbol{\tau}$ is the polymer stress tensor. The polymer molecules are modelled as dumbbells connected by finitely extensible springs. Approximate constitutive equations for this model include the FENE-P equation (Bird

et al. 1987*b*) and the FENE-CR equation (Chilcott & Rallison 1988), which are given in dimensionless form as

$$We_\theta \left(\frac{\partial \boldsymbol{\alpha}}{\partial t} + \boldsymbol{v} \cdot \nabla \boldsymbol{\alpha} - \{\boldsymbol{\alpha} \cdot \nabla \boldsymbol{v}\}^T - \{\boldsymbol{\alpha} \cdot \nabla \boldsymbol{v}\} \right) + \left(\frac{\boldsymbol{\alpha}}{(1 - \mathrm{tr}(\boldsymbol{\alpha})/b)} - \frac{\boldsymbol{I}}{(1 - c_r \, \mathrm{tr}(\boldsymbol{\alpha})/b)} \right) = 0, \tag{2.3}$$

where $\boldsymbol{\alpha}$ is the ensemble average of the polymer conformation tensor, $\boldsymbol{I}$ is the identity tensor, $\sqrt{b}$ is a dimensionless measure of the maximum extensibility of the dumbbells, We_θ is the Weissenberg number, which is the product of the polymer relaxation time and a characteristic shear rate, and c_r is a parameter which takes the value 1 for the FENE-CR model and 0 for the FENE-P model. Values of c_r between 0 and 1 do not correspond to any standard constitutive equation; this parameter merely serves as a convenient way of performing numerical continuation between the FENE-P and FENE-CR equations. Both models are derived by applying approximate closures to the equation governing the evolution of the ensemble average of the conformation tensor of a dilute solution of non-interacting dumbbells connected by nonlinear springs, and are used extensively in numerical calculations. The FENE-P model predicts a shear-thinning viscosity and first normal stress coefficient, whereas the FENE-CR model predicts a shear-thinning first normal stress coefficient but a constant viscosity. Thus, the two models differ in their prediction of the balance between shear and normal stresses. The FENE-P model has been found to better approximate the behaviour of the 'exact' FENE model (Bird *et al.* 1987*b*) in steady shear and elongational flows than the FENE-CR model (Herrchen & Öttinger 1997). Given the differences between the two models, we would expect them to exhibit different behaviour in complex flows, and our computations confirm this.

For both models, b and the components of $\boldsymbol{\alpha}$ are scaled by kT/H, where k is Boltzmann's constant, T is the temperature, and H is the spring constant. Distance is scaled by the gap width, and time by the inverse of a characteristic shear rate. Since the FENE-P model does not yield an analytical solution for the base state in Couette–Dean flow, we take the characteristic shear rate to be the shear rate at the outer cylinder for an Oldroyd-B fluid (infinitely extensible springs, i.e. $1/b = 0$) flowing through the same geometry. The velocity scale is chosen to be the product of the time scale and the gap width. The polymer stress, scaled by the shear modulus η_p/λ, is obtained from $\boldsymbol{\alpha}$ using the relation $\boldsymbol{\tau} = \boldsymbol{\alpha}/(1 - \mathrm{tr}(\boldsymbol{\alpha})/b) - \boldsymbol{I}/(1 - c_r \, \mathrm{tr}(\boldsymbol{\alpha})/b)$. Other parameters of importance are the dimensionless gap width $\epsilon = (R_2 - R_1)/R_2$, and δ, which measures the relative importance of the pressure gradient as the driving force for the flow, given by

$$\delta = \frac{-K_\theta \epsilon^2 R_2/(2\eta_t)}{(1 - \epsilon) R_2 \Omega - K_\theta \epsilon^2 R_2/(2\eta_t)}, \tag{2.4}$$

so that $\delta = 0$ is circular Couette flow and $\delta = 1$ is Dean flow. The velocity satisfies no-slip boundary conditions on the walls of the cylinder.

3. Discretization and solution methods

Equations (2.1), (2.2) and (2.3) form a set of partial differential equations for the three components of the velocity, the pressure, and the six components of $\boldsymbol{\alpha}$. We look for steady, axisymmetric solutions that are periodic in the axial direction with a dimensionless period (scaled by the gap width) of L, so each variable only depends

on two spatial directions, the radial direction r (shifted and scaled so that $r = 0$ is the inner cylinder and $r = 1$ the outer cylinder), and the axial direction z. In performing the numerical discretization, we can take advantage of certain symmetry properties of the solutions we seek. In particular, we take the radial and azimuthal velocities to be reflection symmetric about the plane $z = L/2$, and the axial velocity to be reflection anti-symmetric. This implies that α_{rr}, $\alpha_{r\theta}$, $\alpha_{\theta\theta}$, α_{zz} and p are reflection symmetric, while α_{rz} and $\alpha_{\theta z}$ are reflection anti-symmetric. Thus, the computational domain is $\Gamma = \{0 \leqslant r \leqslant 1,\ L/2 \leqslant z \leqslant L\}$, which is half the size of the physical domain.

Considerable care needs to be exercised when choosing a discretization scheme. Since we are looking for localized solutions, the primary consideration is to choose a scheme which permits efficient local refinement. The spectral element scheme of Patera (1984) satisfies this requirement while also preserving the exponential convergence properties of a global spectral method as long as the solution components in each element are well resolved. Our investigations showed that this method performs much better than either a global Chebyshev/Fourier or Chebyshev/Chebyshev collocation scheme or a domain decomposition Chebyshev/Chebyshev collocation scheme. Additionally, we found that the linear systems associated with the continuation scheme presented below are also better conditioned for a spectral element scheme than for a global spectral method. In the spectral element formulation, we apply Galerkin weighting on the conservation and continuity equations, and streamline-upwind/Petrov-Galerkin weighting (Brooks & Hughes 1982; Marchal & Crochet 1987) on the constitutive equations. The formulation, which is based on the weak form of the governing equations, is given by

$$\int_\Gamma (-p\boldsymbol{I} + \boldsymbol{\tau} + We_\theta S\nabla \boldsymbol{v}) : \nabla \boldsymbol{u}\, \mathrm{d}\Gamma = \int_{\partial\Gamma} \mathbf{u} \cdot (-p\boldsymbol{I} + \boldsymbol{\tau} + We_\theta S\nabla \boldsymbol{v}) \cdot \boldsymbol{n}\, \mathrm{d}s, \quad \forall\, \boldsymbol{u} \in U, \tag{3.1}$$

$$\int_\Gamma q\nabla \cdot \boldsymbol{v}\, \mathrm{d}\Gamma = 0, \quad \forall\, q \in Q, \tag{3.2}$$

$$\int_\Gamma \left(We_\theta \left(\frac{\partial \boldsymbol{\alpha}}{\partial t} + \boldsymbol{v} \cdot \nabla \boldsymbol{\alpha} - \{\boldsymbol{\alpha} \cdot \nabla \boldsymbol{v}\}^T - \{\boldsymbol{\alpha} \cdot \nabla \boldsymbol{v}\} \right) + \frac{\boldsymbol{\alpha}}{(1 - \mathrm{tr}(\boldsymbol{\alpha})/b)} - \frac{\boldsymbol{I}}{(1 - c_r\, \mathrm{tr}(\boldsymbol{\alpha})/b)} \right) : (\boldsymbol{w} + c\boldsymbol{v} \cdot \nabla \boldsymbol{w})\, \mathrm{d}\Gamma = 0, \quad \forall \boldsymbol{w} \in W, \tag{3.3}$$

where $U \in H^1(\Gamma)$, the space of functions whose first derivatives are square integrable over Γ, $W, Q \in L^2(\Gamma)$, the space of functions which are square integrable over Γ, and $c = h/V$ where h is a characteristic length scale of an element, V is a characteristic velocity, and $\boldsymbol{n}$ is the unit normal vector pointing out of the domain. We take h to be the square root of the area of the element, and V to be the average of the magnitude of the velocity at the four corners of each element. Both the interpolating functions and the weighting functions must be chosen to satisfy the symmetry conditions discussed above.

In each element, the variables are approximated by tensor products of Lagrange polynomials defined on the Gauss–Lobatto–Legendre (GLL) grid. We take the symmetry properties into account by treating the elements bordering the axial edges in a different way than the interior elements. Since the GLL grid is defined in the domain $\{-1 \leqslant \xi \leqslant 1\}$, we map each interior element to $\{-1 \leqslant \xi_r \leqslant 1, -1 \leqslant \xi_z \leqslant 1\}$. We map the elements bordering the left-hand edge ($z = L/2$) to the range $\{-1 \leqslant \xi_r \leqslant 1, 0 \leqslant \xi_z \leqslant 1\}$, and use even axial interpolants for the reflection symmetric components and

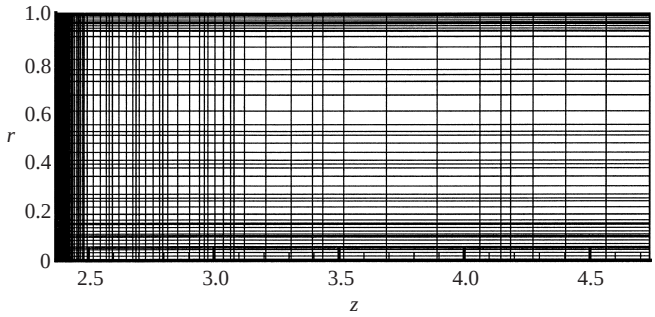

FIGURE 2. A spectral element mesh with 16 axial and 16 radial elements with fifth-order polynomials in each direction in each domain. Note the dense concentration of points near $r = 1$ and $z = L/2$. The high resolution is necessary to capture the intense stress localization in these regions.

odd interpolants for the reflection anti-symmetric components. Similarly, we map the elements bordering the right-hand edge ($z = L$) to $\{-1 \leqslant \xi_r \leqslant 1, -1 \leqslant \xi_z \leqslant 0\}$ and use even or odd interpolants as appropriate. A sample spectral element mesh is shown in figure 2.

In order to avoid spurious pressure modes, the relative approximation orders of velocity and pressure need to satisfy the Ladyzheskaya, Babuska and Brezzi condition. We ensure this by using interpolants for the pressure that are based on a grid that has two fewer points in each direction than the velocity grid in each element. We choose the approximation orders for the components of $\boldsymbol{\alpha}$ to be the same as for the velocity. We perform the integrations in equations (3.1) to (3.3) using Gauss–Legendre quadrature on the GLL grid in each element and construct the final system by direct stiffness summation. This procedure reduces the system of nonlinear partial differential equations to a system of nonlinear algebraic equations for the nodal values of the variables on the appropriate GLL grid in each element. These equations can be written in compact form as

$$\boldsymbol{E}\frac{\partial \boldsymbol{y}}{\partial t} = \boldsymbol{f}(\boldsymbol{y}, We_\theta, S, \epsilon, b, L, \delta). \tag{3.4}$$

The matrix $\boldsymbol{E}$ has zeros in the rows corresponding to the momentum and continuity equations. Steady states correspond to solving

$$\boldsymbol{f}(\boldsymbol{y}, We_\theta, S, \epsilon, b, L, \delta) = \boldsymbol{0}. \tag{3.5}$$

Solutions to equation (3.5) are tracked using a numerical continuation procedure, the starting point for which is the base-state Oldroyd-B solution. This solution is used as an initial guess for the FENE-P or FENE-CR base-state solution and refined using a Newton iteration. We calculate subsequent points along the branch using a pseudo-arclength continuation algorithm (Seydel 1994), which we briefly describe here. Let us denote the set of the values of the variables at the collocation points by the vector $\boldsymbol{y}$, and the continuation parameter by μ. Here, μ could be We_θ, b, or L. In pseudo-arclength continuation, we consider both $\boldsymbol{y}$ and μ to be functions of an arclength parameter s. Thus, we can write the set of discretized equations in the compact form

$$\boldsymbol{f}(\boldsymbol{y}(s), \mu(s)) = \boldsymbol{0}. \tag{3.6}$$

Given a point $(\boldsymbol{y}^0, \mu^0)$ on the solution branch, the idea is to find the next point $(\boldsymbol{y}^1, \mu^1)$ such that, apart from satisfying the governing equations, it obeys an additional

constraint

$$N(\boldsymbol{y}, \mu) = \dot{\boldsymbol{y}}^0 \cdot (\boldsymbol{y} - \boldsymbol{y}^0) + \dot{\mu}^0(\mu - \mu^0) - \Delta s = 0, \tag{3.7}$$

where $(\dot{\boldsymbol{y}}^0, \dot{\mu}^0)$ is the unit tangent at the point $(\boldsymbol{y}^0, \mu^0)$, and Δs is a specified step length. At each step, we use a Newton iteration to solve the augmented set of equations

$$\boldsymbol{f}(\boldsymbol{y}(s), \mu(s)) = \boldsymbol{0}, \quad N(\boldsymbol{y}(s), \mu(s)) = 0. \tag{3.8}$$

The Jacobian matrix of this system is given by

$$\boldsymbol{J} = \begin{pmatrix} \boldsymbol{f}_y & \boldsymbol{f}_\mu \\ \dot{\boldsymbol{y}}^0 & \dot{\mu}^0 \end{pmatrix} \tag{3.9}$$

and is not singular at a turning point.

While tracing a solution branch, we check for stationary bifurcations using a test function method (Seydel 1994). The test function is a scalar function that changes sign at a stationary bifurcation point, and is relatively inexpensive to compute. Suppose that $(\boldsymbol{f}_y^0, \mu^0)$ is a stationary bifurcation point. Then, it follows that

$$\boldsymbol{f}_y(\boldsymbol{y}^0, \mu^0)\boldsymbol{h} = \boldsymbol{0}, \tag{3.10}$$

where $\boldsymbol{h}$ is the eigenvector corresponding to the zero eigenvalue of $\boldsymbol{f}_y(\boldsymbol{y}^0, \mu^0)$. Suppose now that we are at a point $(\bar{\boldsymbol{y}}, \bar{\mu})$ different from the bifurcation point. Then equation (3.10) with $(\boldsymbol{y}^0, \mu^0)$ replaced by $(\bar{\boldsymbol{y}}, \bar{\mu})$ has no non-trivial solution for $\boldsymbol{h}$. However, we can get a solution to an equation that resembles this closely. We arbitrarily choose two indices l and k, and require that $h_k = 1$. We do this by replacing the lth row in equation (3.10) by the equation $\boldsymbol{e}_k^T \boldsymbol{h} = 1$, where $\boldsymbol{e}_k$ is the column vector with a 1 in the kth position and zeros elsewhere. After this substitution, equation (3.10) becomes

$$\boldsymbol{J}_{lk}\boldsymbol{h} = \boldsymbol{e}_l, \tag{3.11}$$

where $\boldsymbol{J}_{lk}$ is the matrix obtained after performing the indicated substitutions in $\boldsymbol{f}_y$. If we are exactly at the bifurcation point, then $\boldsymbol{h}$ is simply the eigenvector corresponding to the zero eigenvalue, normalized so that its kth component is 1. If equation (3.11) is solved close to a bifurcation point, then $\boldsymbol{h}$ is a good approximation to the eigenvector corresponding to the zero eigenvalue. In particular, the scalar function

$$t_{lk} = \boldsymbol{e}_l^T \boldsymbol{f}_y(\boldsymbol{y}, \mu)\boldsymbol{h} \tag{3.12}$$

is zero at a bifurcation point, and changes sign as a bifurcation point is crossed. We use t_{lk} with $l = k$ to check for stationary bifurcations.

If a stationary bifurcation is detected, as for example when the trivial branch in Dean flow becomes unstable, we need to begin tracking the new branch. To compute a first approximation to a point on the new branch, we use the fact that $\boldsymbol{h}$ closely approximates the eigenvector corresponding to the zero eigenvalue, and write

$$\bar{\boldsymbol{z}} = \bar{\boldsymbol{y}} + \delta^0 \boldsymbol{h}, \tag{3.13}$$

for some small value of δ^0, as an approximation to a point on the new branch. However, if we perform a Newton iteration starting with $\bar{\boldsymbol{z}}$ as the initial guess, we are likely to converge back to the old branch. Instead, we perform a Newton iteration on the augmented system of equations

$$\begin{pmatrix} \boldsymbol{f}(\boldsymbol{z}, \mu) \\ z_k - \bar{z} \end{pmatrix} = \boldsymbol{0} \tag{3.14}$$

to solve for a point $(\boldsymbol{z}^*, \mu^*)$ on the new branch. In equation (3.14), we are simply specifying the value of a solution component on the new branch and solving for the point $(\boldsymbol{z}^*, \mu^*)$ where this holds. The method is especially effective when switching from the base solution to the non-trivial branch because we can choose k to be a component of v_r or v_z, both of which are zero in the base state.

The test function approach allows us to determine the existence of stationary bifurcations. To determine stability with respect to oscillatory disturbances, we need to find the eigenvalues ω of the generalized eigenvalue problem

$$\boldsymbol{f}_{\boldsymbol{y}}\,\boldsymbol{q} = \omega \boldsymbol{E}\,\boldsymbol{q}. \tag{3.15}$$

If any of the eigenvalues have positive real parts, the solution is unstable with respect to disturbances that have the same symmetry properties that $\boldsymbol{y}$ has and have wavelengths L^* such that L/L^* is an integer; otherwise it is stable with respect to such disturbances. We do not attempt the much more demanding task of determining stability with respect to disturbances of arbitrary wavelength. Since we are only interested in determining stability, we do not need to find the entire spectrum of eigenvalues. It is only necessary to check if any of the ω have positive real parts. To do this, we use an Arnoldi scheme, as implemented in the public domain software package ARPACK (Lehoucq, Sorensen & Yang 1997), to calculate a few such eigenvalues. Since ARPACK does not have a built-in option to calculate a specified number of eigenvalues with positive real parts, we use a spectral transformation suggested by Christodoulou & Scriven (1988). Using this transformation, we find the eigenvalues κ of the matrix $\boldsymbol{P} = (\boldsymbol{E} - \boldsymbol{f}_{\boldsymbol{y}})^{-1}(\boldsymbol{E} + \boldsymbol{f}_{\boldsymbol{y}})$. These eigenvalues are related to the the eigenvalues ω in equation (3.15) by means of the transformation

$$\kappa_i = \frac{1 + \omega_i}{1 - \omega_i}. \tag{3.16}$$

The eigenvectors of $\boldsymbol{P}$ are identical to those of equation (3.15). This transformation maps the eigenvalues in the left-half of the complex plane to the interior of the unit circle. Thus, the eigenvalues of equation (3.15) with positive real parts map on to the eigenvalues of $\boldsymbol{P}$ with the largest magnitude, and are easily found by ARPACK. We should mention here that the Arnoldi scheme constructs a Krylov subspace by the successive action of $\boldsymbol{P}$ on a vector. As is evident from the definition of $\boldsymbol{P}$, the construction of each such vector requires the solution of a linear system. Thus, the eigenvalue computation is an expensive process, and we only perform it for a few points.

The process for determining stability with respect to non-axisymmetric modes is somewhat more complicated. We write the solution vector $\boldsymbol{\phi}$ as

$$\boldsymbol{\phi}(r, z, \theta) = \bar{\boldsymbol{\phi}}(r, z) + \hat{\epsilon}\tilde{\boldsymbol{\phi}}(r, z)\exp(\omega t + \mathrm{i}n\theta), \tag{3.17}$$

where $\hat{\epsilon}\tilde{\boldsymbol{\phi}}$ is a small perturbation, ω is the growth rate, and n is the azimuthal wavenumber of the perturbation, which is an integer. Substituting this in the governing equations, and retaining terms at $O(\hat{\epsilon})$ gives a complex generalized problem for the growth rate ω:

$$\boldsymbol{J}\tilde{\boldsymbol{\phi}} = \omega\,\boldsymbol{E}\,\tilde{\boldsymbol{\phi}}. \tag{3.18}$$

As in the axisymmetric case, we can reduce this to a regular eigenvalue problem using the spectral transformation $\boldsymbol{K} = (\boldsymbol{E} - \boldsymbol{J})^{-1}(\boldsymbol{E} + \boldsymbol{J})$.

At this point, it is clear that every step of the procedure involves the solution of a

system of linear equations. Let us denote the generic equation we solve as

$$\boldsymbol{A}\boldsymbol{x} = \boldsymbol{b}. \tag{3.19}$$

It is well worth expending effort to make the solution process efficient. First, $\boldsymbol{A}$ is a sparse matrix, so considerable savings in memory result from just storing the non-zero entries together with integer pointer arrays that store information about the coordinates of each stored entry. The sparse nature of $\boldsymbol{A}$ also means that a properly implemented iterative method could be more efficient at solving equation (3.19) than a direct scheme. The iterative scheme we use is GMRES (Saad & Schultz 1986). However, GMRES will converge only if $\boldsymbol{A}$ is well conditioned, and this is generally far from being true for the systems we solve. Therefore, we solve a preconditioned system

$$\boldsymbol{M}\,\boldsymbol{A}\,\boldsymbol{x} = \boldsymbol{M}\boldsymbol{b}, \tag{3.20}$$

where $\boldsymbol{M}$ is an approximation to $\boldsymbol{A}^{-1}$. The preconditioner that we use is a modified version of incomplete LU decomposition with dual threshold (ILUT) to control fill in (Saad 1996). To build this preconditioner, we construct an auxiliary matrix $\tilde{\boldsymbol{A}}$ by setting to zero in $\boldsymbol{A}$ the entries corresponding to the velocities and pressure in the rows corresponding to the constitutive equation, and the entries corresponding to the components of $\boldsymbol{\alpha}$ in the rows corresponding to the momentum and continuity equations. We then construct an ILUT decomposition of $\tilde{\boldsymbol{A}}$ and apply this as a preconditioner for $\boldsymbol{A}$, denoting this method ILUT*. We find that this is a very effective technique, and the largest linear systems that we have solved ($O(60\,000)$ unknowns) converge to a relative accuracy of 10^{-6} in about 350 GMRES iterations, with the preconditioner having about three times the number of non-zero entries that $\boldsymbol{A}$ does. Smaller systems converge faster and fewer non-zero entries can be kept in the preconditioner.

In using ILUT* to solve the complex generalized eigenvalue problem indicated by equation (3.18), we need to modify the problem so that it only involves real numbers. Recall that the spectral transformation requires the solution of the linear system

$$(\boldsymbol{E} - \boldsymbol{J})\,\boldsymbol{x} = \boldsymbol{b} \tag{3.21}$$

for each iteration of ARPACK. Instead, we rewrite equation (3.18) as a real-valued problem

$$\omega \begin{pmatrix} \boldsymbol{E} & \boldsymbol{0} \\ \boldsymbol{0} & \boldsymbol{E} \end{pmatrix} \begin{pmatrix} \tilde{\boldsymbol{\phi}}_r \\ \tilde{\boldsymbol{\phi}}_i \end{pmatrix} = \begin{pmatrix} \boldsymbol{J}_r & \boldsymbol{J}_i \\ \boldsymbol{J}_i & \boldsymbol{J}_r \end{pmatrix} \begin{pmatrix} \tilde{\boldsymbol{\phi}}_r \\ \tilde{\boldsymbol{\phi}}_i \end{pmatrix}, \tag{3.22}$$

where the subscripts r and i denote respectively the real and imaginary parts of the vector or matrix. Note that the matrix $\boldsymbol{E}$ is purely real and hence does not have a subscript. The spectral transformation now requires the solution of linear systems involving the matrix

$$\boldsymbol{S} = \begin{pmatrix} (\boldsymbol{E} - \boldsymbol{J})_r & -\boldsymbol{J}_i \\ \boldsymbol{J}_i & (\boldsymbol{E} - \boldsymbol{J})_r \end{pmatrix},$$

which is real. To precondition this matrix, we note that the matrix $\boldsymbol{J}_i$ has far fewer entries than $(\boldsymbol{E}-\boldsymbol{J})_r$. Therefore, as a first approximation, we can neglect it in computing the preconditioner. We construct the preconditioner by performing ILUT* on $(\boldsymbol{E}-\boldsymbol{J})_r$. If $\boldsymbol{M}^*$ represents this decomposition, we precondition $\boldsymbol{S}$ using the matrix

$$\begin{pmatrix} \boldsymbol{M}^{*-1} & \boldsymbol{0} \\ \boldsymbol{0} & \boldsymbol{M}^{*-1} \end{pmatrix}.$$

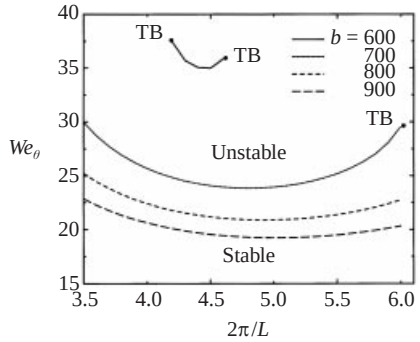

FIGURE 3. Linear stability curves at $\delta = 1$ (Dean flow) computed using the FENE-P model. The points marked TB are Takens–Bogdanov points. The lines correspond to points where the base-state flow loses stability to stationary axisymmetric perturbations.

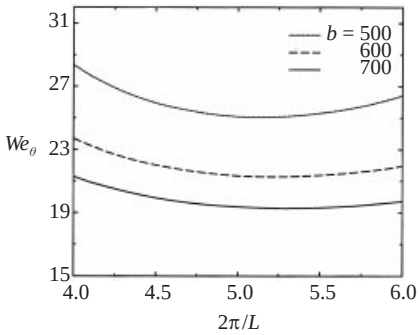

FIGURE 4. Linear stability curves at $\delta = 1$ (Dean flow) computed using the FENE-CR model. As in figure 3, only stationary axisymmetric perturbations are considered. Note the complete absence of non-stationary bifurcations.

4. Results and discussion

4.1. *Stationary bifurcations from the Dean and Couette–Dean flows*

Rather than explore large volumes of parameter space, we restrict our attention to values close those used in the experiments by Groisman & Steinberg (1997). Specifically, we fix the value of S at 1.2, and except when we examine the effect of varying the gap width, set $\epsilon = 0.2$. These values are close to the ones used in the experiments by Groisman & Steinberg (1997). For most of our work, we use the FENE-P model. The reasons for this choice will become clear later in this section. For now, we simply note that the polyacrylamide solutions used in the experiments showed shear thinning in both the viscosity and the first normal stress coefficient (Groisman & Steinberg 1998), which indicates that the FENE-P constitutive equation may be a better model for these solutions than the FENE-CR equation.

In order to track stationary non-trivial branches, it is first necessary to find from where they bifurcate. Therefore, the logical starting point of our investigation is the linear stability diagram for Dean flow. Figure 3 shows such a diagram computed using the FENE-P model. Takens–Bogdanov points, where the bifurcation switches from a stationary mode to an oscillatory mode, are marked TB. Unlike in the Oldroyd-B model, where one such point is seen only at very small wavelengths (Ramanan *et al.* 1999), as the polymer becomes stiffer (i.e. b decreases), these points are shifted to larger

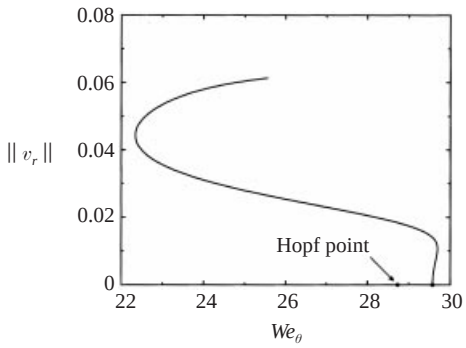

FIGURE 5. Continuation in We_θ of a stationary solution in Dean flow. The parameter values are $L = 1.05$, $b = 700$, $\epsilon = 0.20$, and $S = 1.2$. At the Hopf point, a pair of complex conjugate eigenvalues becomes unstable. These collide and form two real eigenvalues, one of which recrosses the imaginary axis at $We_\theta = 29.57$, where the stationary branch originates. The solution amplitude used here differs from that used in subsequent figures and is defined in equation (4.1).

wavelengths. For a sufficiently small value of b, there is no stationary bifurcation from the base state at all. From the point of view of numerical simulation, we would prefer to work with as small a value of b as possible, expecting stress boundary layers to be less sharp for smaller values of b, which in turn makes the computations easier. However, decreasing b tends to lower the elastic character of the fluid and suppresses elastic instabilities. Before moving on to the non-trivial solutions, we present some linear stability results for Dean flow of the FENE-CR model in figure 4. Note that, unlike in the FENE-P model, stationary bifurcations are seen even at low values of b. Thus, the FENE-CR model predicts linear stability behaviour that is qualitatively different from that predicted by the FENE-P model. We will have more to say on the differences between the two models in § 4.3.

4.2. *The branch structure of viscoelastic Couette–Dean flows*

We begin the nonlinear analysis by tracking the bifurcating branch of stationary solutions in Dean flow at $b = 700$ and $L = 1.05$. Since this value of b is relatively small, numerical continuation is not difficult and a crude numerical scheme suffices. We performed these calculations using a global Chebyshev collocation scheme in both the radial and axial directions. At $L = 1.05$, a pair of complex conjugate eigenvalues crosses the imaginary axis at $We_\theta = 28.73$. Upon further increasing We_θ, the two unstable eigenvalues coalesce and form a pair of unstable real eigenvalues which then move in opposite directions. The smaller one of these recrosses the imaginary axis at $We_\theta = 29.57$. We track in We_θ the stationary branch bifurcating as result of this crossing. The result is shown in figure 5, where we plot the solution amplitude, measured by the quantity

$$\| v_r \| = \left(\sum_{i=0}^{N_r} \sum_{j=0}^{N_z} |v_{r,ij}|^2 \right)^{1/2}, \tag{4.1}$$

as a function of We_θ, where $N_r + 1$ and $N_z + 1$ are the number of Chebyshev collocation points used in the radial and axial directions respectively. We see that the bifurcation is mildly supercritical, but quickly turns back and shows a marked hysteretic character. The turning point at $We_\theta = 22.34$ is much lower than the value of 28.73 where the base solution loses stability. When we pick a point on this branch

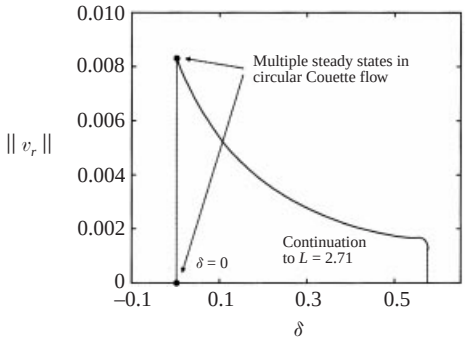

FIGURE 6. A path to non-trivial stationary solutions in circular Couette flow. The parameters are $We_\theta = 25.15$, $L = 3.07$, $b = 1830$, $\epsilon = 0.2$, and $S = 1.2$.

and continue it down in δ we find, however, that it does not extend all the way to $\delta = 0$. For instance, picking $We_\theta = 23.35$ on the upper branch in figure 5 and tracking it in δ, we find that the branch turns back at $\delta = 0.69$. We have tried this for other points as well, but in all cases, they turn back well before reaching $\delta = 0$. Therefore, at least for this value of b and L, there is no direct path from non-trivial solutions in Dean flow to those (if any) in circular Couette flow.

Given the apparent absence of a direct route from $\delta = 1$ to $\delta = 0$, we focused on smaller values of δ and larger values of b and L. As b increases, the solutions become more localized, and the global scheme we originally used is inefficient. Hence, we switched to the spectral element/SUPG method described in § 3. At $b = 1830$, $\delta = 0.576$, and $L = 2.71$, a stationary bifurcation occurs at $We_\theta = 25.15$. We tracked the bifurcating branch at this value of We_θ up to $L = 3.07$ and then down in δ. This path is shown in figure 6. The velocity norm used in this and all subsequent figures is defined as

$$\| v_r \| = \left(\int_\Gamma v_r^2 \, \mathrm{d}\Gamma \right)^{1/2}. \tag{4.2}$$

As figure 6 shows, this branch exists all the way to $\delta = 0$. This computation demonstrates that an isolated branch of non-trivial solutions does indeed exist in the circular Couette geometry.

4.3. *Non-trivial stationary solutions in Couette–Dean flow – Diwhirls*

Having computed a stationary solution at $\delta = 0$, we can determine the effect of changing various parameters. The first parameter we focus on is the wavelength. The results of continuing our solution at $We_\theta = 25.15$ in L are shown in figure 7. The upper branch, being a stronger flow, is much harder to track than the lower branch, and the end point of this branch represents the largest value of L at which we could obtain converged solutions on the upper branch for this value of We_θ. The lower branch presents fewer problems and we were able to track it with relative ease. The key observation from figure 7 is that as L increases, both the lower and upper branches become flat, suggesting that the spatial patterns are becoming independent of the size of the computational domain, i.e. they are becoming localized. Examination of the solution components confirmed that this was indeed the case, with the localization occurring in the region near $z = L/2$. Since the components of the solution show little or no axial variation far away from $z = L/2$, we can simply use their values at the nodal points for a lower value of L as an initial guess for the solution at a larger

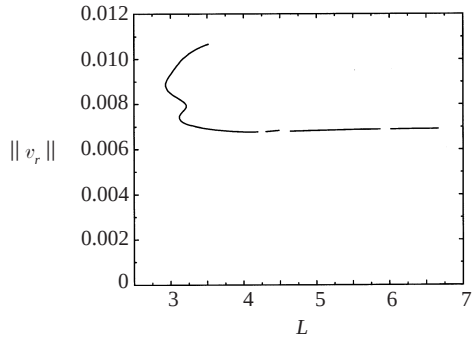

FIGURE 7. Results from continuing the stationary circular Couette flow solutions in L. The parameters are $We_\theta = 25.15$, $b = 1830$, $\epsilon = 0.2$, and $S = 1.2$. The gaps in the lower branch correspond to places where we changed the mesh. Note the flatness of the branches as L increases. We have computed extensions of the upper branch at lower values of We_θ.

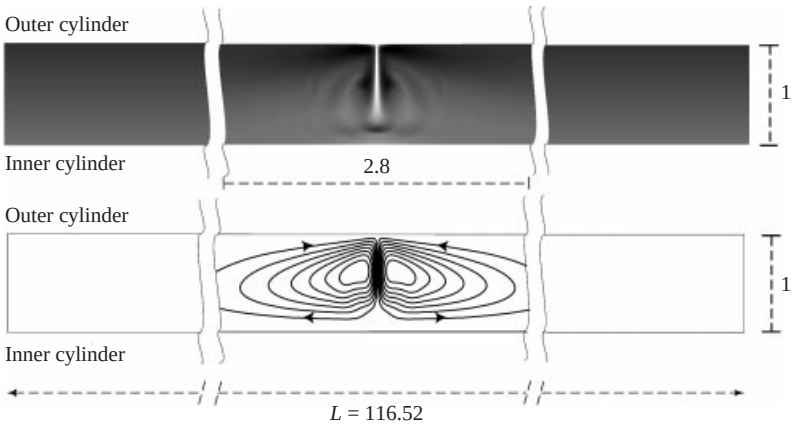

FIGURE 8. Density plot of $\alpha_{\theta\theta}$ (white is large stretch, black small) and contour plot of the streamfunction at $L = 116.52$ ($We_\theta = 24.29$, $b = 1830$, $S = 1.2$, and $\epsilon = 0.2$). For clarity, most of the flow domain is not shown. Note the very strong localization of $\alpha_{\theta\theta}$ near the centre. The maximum value of $\alpha_{\theta\theta}$ at the core is 1589 which gives $\tau_{\theta\theta} = 12722$. Compared to this, the maximum value of $\alpha_{\theta\theta}$ in the circular Couette base state is 706, which gives $\tau_{\theta\theta} = 1150$. Away from the core of the diwhirl, the structure is pure circular Couette flow. The streamlines show striking similarity to those in figure 10 of Groisman & Steinberg (1998).

value of L, while increasing the axial extent of the domains bordering the edges (i.e. $z = L$). This method of remeshing captures the localization effectively and avoids the necessity of computing solutions at intermediate values of L. Using this technique, we were able to get converged solutions on the lower branch for wavelengths that are in excess of 100 times the width of the gap between the cylinders. We have also used this technique to compute such long-wavelength solutions on the upper branch at lower values of We_θ. We show the results of one such computation in figure 8. This figure shows the streamfunction contours and a density plot of $\alpha_{\theta\theta}$ at $L = 116.52$ and $We_\theta = 24.29$ on the upper branch. For clarity, we only show the centre and edges of the domain. The streamfunction contours are strongly localized near the centre of the flow cell, which is a region of very strong inflow. Away from the core is a region of weak outflow, and even further away, the solution is pure circular Couette flow. The $\alpha_{\theta\theta}$ field shows an even stronger localization. It is the necessity of capturing this

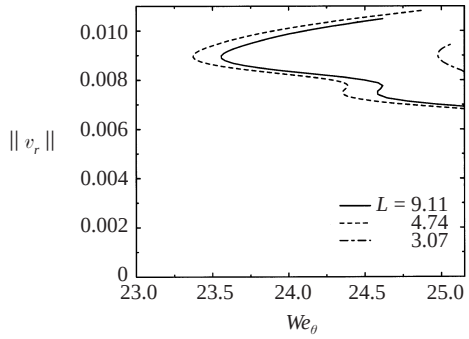

FIGURE 9. Diwhirl solution amplitudes as functions of We_θ and L. Note that the curves at $L = 9.11$ and $L = 4.74$ are very close together, and well separated from the curve at $L = 3.07$ ($b = 1830$, $S = 1.2$, and $\epsilon = 0.2$).

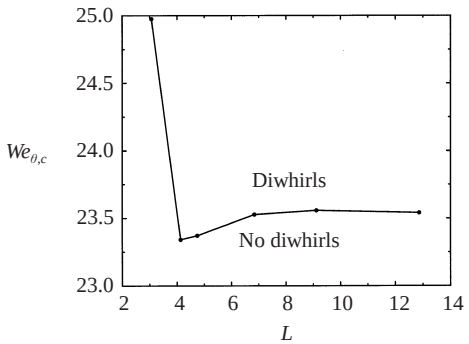

FIGURE 10. Plot of the location of the turning point, $We_{\theta,c}$, versus L at $S = 1.2$ and $\epsilon = 0.2$. Note the flatness of the curve at large L.

strong localization that requires the use of a numerical method that permits efficient local refinement. The streamlines at the core are remarkably similar to those in figure 10 on p. 2457 of Groisman & Steinberg (1998). Henceforth, we will call our solutions diwhirls as well.

Figure 9 shows the results of continuation in We_θ for solutions at three different values of L. All three curves show turning points in We_θ, i.e. there is a lower limit in We_θ below which the diwhirls are not seen. Note that the curves at $L = 9.11$ and 4.74 are close together, and are both well separated from the curve at $L = 3.07$. This further highlights the independence of the solutions of L for large enough L.

In figure 10, we show a plot of the location of the turning point in Weissenberg number ($We_{\theta,c}$) as a function of the wavelength. The most interesting feature in figure 10 is the flatness of the curve at large L, indicating yet again that, for large L, the characteristics of the solution are independent of the wavelength. Another interesting feature in figure 10 is that the curve shows a minimum, i.e. the diwhirl patterns exhibit wavelength selection. This minimum, which occurs at a Weissenberg number of approximately 23.3, is therefore the lowest Weissenberg number at which the FENE-P model with the chosen parameters predicts diwhirls to occur. More important than the absolute value is the relative position of the turning point and linear stability limits. The base-state circular Couette flow is unstable with respect to axisymmetric disturbances above $We_\theta = 20.37$ – all the solutions that we compute

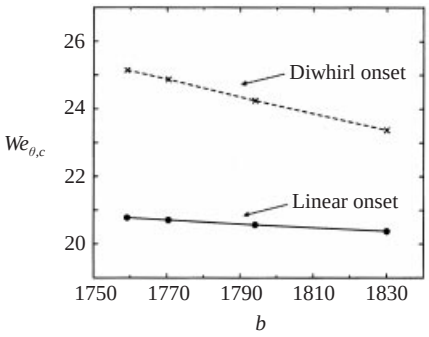

FIGURE 11. Plot of the position of the linear stability limit in circular Couette flow with respect to axisymmetric disturbances and the turning point in We_θ for the diwhirls as a function of b. The parameters are $S = 1.2$ and $\epsilon = 0.2$. The computations for the diwhirls were performed at $L = 4.74$, which is close to the minimum in figure 10.

lie above the linear stability limit of circular Couette flow. In contrast, Groisman & Steinberg (1998) observe diwhirls at Weissenberg numbers as low as 10, well below the linear stability limit of the base flow. One reason for this discrepancy could be the approximate nature of the FENE-P model. Yet another could be that our numerical simulations have not been able to access a sufficiently high value of b – the GMRES iterations fail to converge at very large b. In figure 11, we plot the position of the turning point in We_θ as a function of b for $L = 4.74$, which is close to the minimum in figure 10. Also plotted in the figure is the minimum critical value of We_θ at which the base-state circular Couette flow loses stability with respect to axisymmetric perturbations. This figure shows that as b increases, the position of the turning point shifts to lower Weissenberg numbers at a faster rate than the shift in the minimum of the linear stability curve. This result is not unexpected, because the polymer molecules are much more highly stretched in the core of the diwhirl than in the base-state. Therefore, we would expect the nonlinearity of the FENE-P spring law to have a greater effect on the diwhirls than on the base-state Couette flow. It is conceivable, based on the results shown in figure 11, that the two curves would cross at larger values of b (which we are not able to access due to limitations in the numerical scheme) and that the diwhirls would come into existence below the linear stability limit of the base flow. We point out here that Baumert & Muller (1999) and Groisman & Steinberg (1997) performed their experiments with very high molecular weight polymers, for which the values of b are likely to be much higher than we have been able to access in our simulations.

We now present a rough quantitative comparison of our patterns with those from the experimental observations of Groisman & Steinberg (1998). In figure 9 of their paper Groisman & Steinberg present the radial velocity profile as a function of z at a constant radial position near the middle of the gap, where v_r has maximum amplitude. To compare our results with this figure, we chose a point on the upper branch of the curve for $L = 4.74$ with $We_\theta = 23.50$ in figure 9 of this work. We then converted our radial velocity into dimensional units by using values for the physical parameters from Groisman & Steinberg (1998). Specifically, the values we used were $\lambda = 1$ s and $R_2 = 41$ mm. For $\epsilon = 0.2$ used in our computations, this gives a gap width of 8.2 mm, slightly higher than the 7 mm gap used in the experiments. In figure 12, we present a profile of the radial velocity as a function of z for $r = 0.6$, where the radial velocity is maximum. The peak inflow velocity we find is 5.9 mm s^{-1}, which should

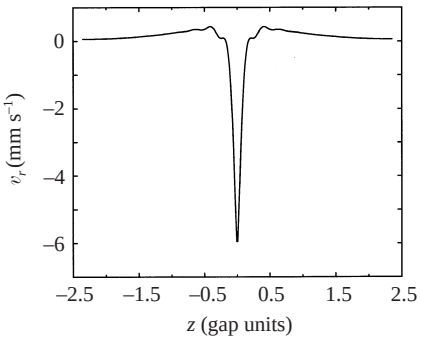

FIGURE 12. The axial variation of v_r at $r = 0.6$ for $L = 4.74$ and $We_\theta = 23.50$ on the upper branch. This figure should be compared to figure 9 on p. 2457 of Groisman & Steinberg (1998). We have shifted the axial coordinate so that the symmetry axis of the diwhirl is at $z = 0$ as in the figure in Groisman & Steinberg (1998).

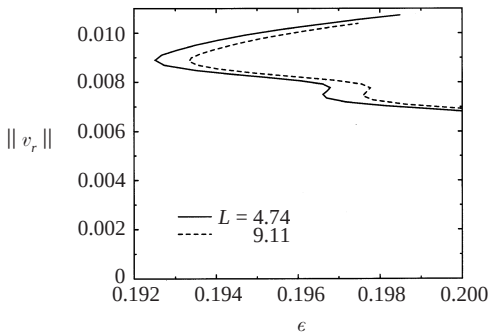

FIGURE 13. Variation of solution amplitudes with ϵ. Here, $We_\theta = 25.15$, and the other parameters are as in figure 9.

be compared to the value of 3.8 mm s^{-1} that Groisman & Steinberg (1998) show in their figure 9. The similarity between these two values is remarkable, more so when we consider how simple the FENE-P model is, and that the Weissenberg number used in figure 12 is roughly twice that at which Groisman & Steinberg (1998) report their results, which means a larger radial velocity should be expected. Furthermore, the wiggles at the shoulders of the peak are not numerical artifacts; similar features are also seen in the experiments.

The dimensionless gap width or curvature ϵ plays a critical role in generating elastic instabilities. Based on the generic mechanism of elastic instabilities, we expect a decrease in curvature to have a stabilizing effect, i.e. keeping other parameters fixed we would expect the diwhirl pattern to vanish at small enough values of ϵ. In figure 13, we show the dependence of the diwhirl solution amplitudes on ϵ. In agreement with expectations, we observe turning points as ϵ decreases. The role of streamline curvature will become clear in § 4.4 where we propose a mechanism for the diwhirls.

As mentioned in § 1, an important reason for attempting to numerically simulate experimentally observed flow patterns is to determine whether a constitutive equation can model complex flows of viscoelastic liquids. Both the FENE-P and the FENE-CR equations are derived by applying closures to the evolution equation for $\boldsymbol{\alpha}$ for a dilute solution of non-interacting dumbbells connected by nonlinear springs. However, the

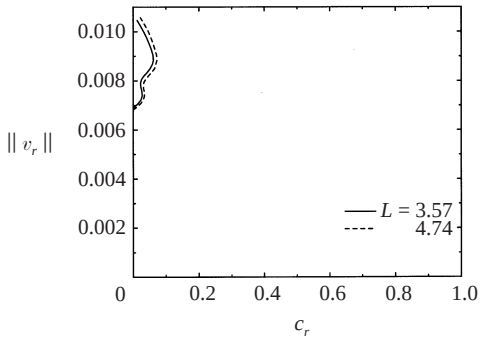

FIGURE 14. Diwhirl solution amplitudes as a function of the parameter c_r for two different wavelengths. $We_\theta = 25.15$ and the other parameters are as in figure 9. The existence of turning points demonstrates that these solutions cannot be extended to the FENE-CR model at the chosen value of b.

'exact' FENE model is better approximated by the FENE-P model (Herrchen & Öttinger 1997). We have already seen that the linear stability curves predicted by the FENE-P and FENE-CR models show significant differences, and we have seen that the FENE-P model equation has stationary solutions in circular Couette flow, which indicates that it is able to capture, at least qualitatively, the mechanism behind the diwhirls. A natural question to ask is whether the FENE-CR model can do so as well. To this end, we perform a continuation of the diwhirl solutions in the parameter c_r, starting from the FENE-P solutions ($c_r = 0$). If the solutions persist at $c_r = 1$, then we will have obtained solitary solutions for the FENE-CR model in circular Couette flow. Figure 14 shows the results of these computations. Both values of L that we chose exhibit turning points at small values of c_r, indicating that these solutions do not exist for the FENE-CR model, at least for the parameter values that we have chosen. As $b \to \infty$, however, the FENE-P and FENE-CR models both collapse to the Oldroyd-B model, so we do expect that for sufficiently large b the FENE-CR model will also exhibit diwhirls.

4.4. *Self-sustaining mechanism*

Since there is no stationary bifurcation in circular Couette flow, the diwhirl solutions that we have computed are part of an isolated branch that does not connect directly to the base state. Therefore, the sustaining mechanism for these patterns must be inherently nonlinear. Groisman & Steinberg (1998) proposed one such mechanism, arguing that the difference in symmetry between inflow and outflow results in the elastic forces performing net positive work on the fluid. While this argument shows that finite-amplitude stationary structures that exhibit significant asymmetry between inflow and outflow are physically plausible, it does not explain the mechanism by which such structures sustain themselves. Having the detailed velocity and stress fields available to us from our computations, we propose a more complete mechanism. Figure 15(*a*) shows a vector plot of $\boldsymbol{v}$ at the axial centreline of the vortex. The figure shows that the azimuthal velocity is increased compared to the base state. The principal components of the stress (figure 15*b*) show that there is an unstable stratification of stress for $r \lesssim 0.99$, i.e. polymer molecules near the outer cylinder are more highly stretched. The inward radial force exerted by the polymers due to this stratification can be seen by examining the radial component of $\nabla \cdot \boldsymbol{\tau}$, which we observe to be strongly negative near the outer cylinder at the core of the diwhirl. This

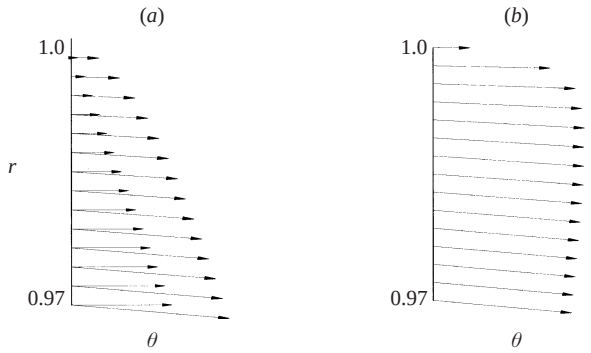

FIGURE 15. (*a*) Vector plot of $\boldsymbol{v}$ near the outer cylinder at the centre of the diwhirl structure (oblique arrows) and the base state (straight arrows). The length of the arrows is proportional to the magnitude of the velocity. The axial velocity is identically zero in the base state, and is zero by symmetry at the centre of the diwhirl. (*b*) Principal stress directions at the same location as for (*a*). The Couette flow stress is not shown because it is very small in comparison. This figure shows how fluid elements at larger radii are pulled down and forward sustaining the increase in v_θ.

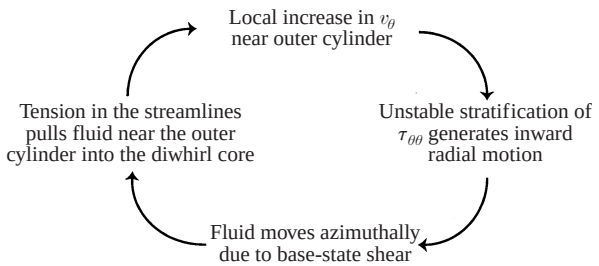

FIGURE 16. Nonlinear self-sustaining mechanism for the diwhirl patterns.

allows us to propose the following fully nonlinear mechanism for the diwhirls (see figure 16): a finite-amplitude perturbation near the outer cylinder results in a local increase in the azimuthal velocity. This in turn creates an unstable stratification of stress, as arises in the base state of Dean flow, which drives inward radial motion. As the fluid moves downward, it is pulled azimuthally due to the shear generated by the motion of the inner cylinder. The tension in streamlines then pulls the fluid at larger radii (i.e. close to the outer cylinder) first axially into the diwhirl core, then forward and down, maintaining the increase in the azimuthal velocity and the large azimuthal normal stresses near the outer cylinder, and resulting in a self-sustaining mechanism. The inward radial motion and azimuthal acceleration, as well as the large degree of stretching that the polymer molecules undergo as they move axially and radially inward, is shown quite dramatically in figure 17, where we have plotted particle paths shaded according to polymer extension ($\mathrm{tr}(\boldsymbol{\alpha})$) near the core of the diwhirl. This mechanism is analogous to that which drives the well-known viscoelastic phenomenon of the tubeless siphon (Bird, Armstrong & Hassager 1987*a*), where large tensile stresses sustain the flow by pulling fluid up from the reservoir when the tip of the siphon tube is raised above the level of the fluid in the container.

4.5. *Stability*

We now address the question of the stability of the diwhirl patterns with respect to axisymmetric and non-axisymmetric disturbances. We determine stability by finding

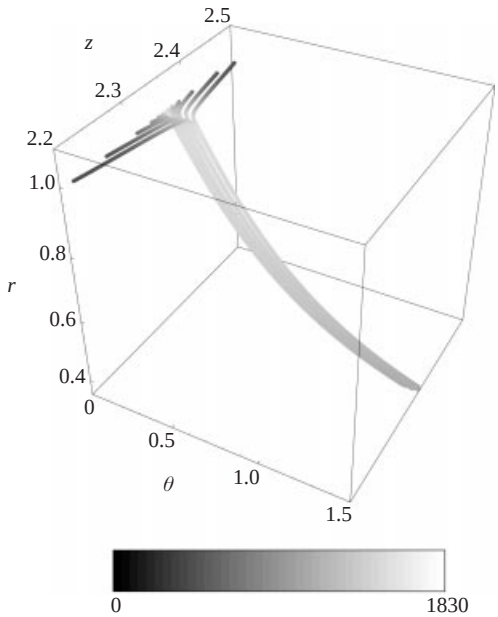

FIGURE 17. Particle paths near the core of the diwhirl ($z = 2.37$), shaded by levels of tr($\boldsymbol{\alpha}$). The paths were generated by starting at $r = 0.99$, $\theta = 0$, and different values of z and integrating to obtain the position at later times. Note the strong extensional flow near the diwhirl core, which combines with the radial inward motion to generate an effect like the tubeless siphon.

the eigenvalues ω in equation (3.15) or (3.18) for non-axisymmetric perturbations. These computations are expensive, so we only perform them for a few points along the upper branch for $L = 4.74$ in figure 9. Here, we report the results from one such computation, performed at $We_\theta = 23.87$. To resolve this point, we needed 16 radial elements and 14 axial elements using fifth-order polynomials in both directions in each element, which is a slightly coarser mesh than the one shown in figure 2, and results in a system with over 53 000 unknowns. The computation requires the storage of two sparse matrices, the preconditioner for one linear system, and the Krylov basis. We used a 600 vector basis (ARPACK would not converge if significantly fewer vectors were used) and asked for the most unstable eigenvalues.

For axisymmetric disturbances, we found two pairs of complex conjugate eigenvalues that had positive real parts. The eigenvectors corresponding to one pair had an irregular grid-scale structure, suggesting that they are part of the continuous spectrum of eigenvalues (Graham 1998; Wilson, Renardy & Renardy 1999; Renardy 2000). These modes are expected to be stable, but since the eigenvectors are non-integrable (Graham 1998), they will not converge exponentially in a spectral element scheme and can display spurious instability. The structure of the other two eigenvectors is shown in figure 18. It shows that although the branch is unstable, the destabilizing disturbance has significant amplitude only near the ends of the domain, where the flow is essentially circular Couette flow. The base circular Couette flow has a minimum critical We_θ of 20.37 with respect to axisymmetric disturbances, and so is linearly unstable at $We_\theta = 23.87$. Hence, it is not surprising that the portion of flow pattern where the flow is essentially circular Couette would be susceptible to destabilizing disturbances. What is interesting, however, is that the core of the pattern, where the diwhirl lies, is entirely unaffected. This shows that the diwhirl pattern is dynamically

	$n = 1$	$n = 2$
1	$3.878 \times 10^{-2} \pm 9.276 \times 10^{-3}\,\mathrm{i}$	$3.674 \times 10^{-2} \pm 1.742 \times 10^{-3}\,\mathrm{i}$
2	$3.590 \times 10^{-2} \pm 1.843 \times 10^{-2}\,\mathrm{i}$	$2.968 \times 10^{-2} \pm 8.189 \times 10^{-2}\,\mathrm{i}$
3	$3.279 \times 10^{-2} \pm 4.878 \times 10^{-2}\,\mathrm{i}$	$2.788 \times 10^{-2} \pm 5.722 \times 10^{-5}\,\mathrm{i}$

TABLE 1. Growth rates ω for the unstable non-axisymmetric modes at $We_\theta = 23.87$, $L = 4.74$, $S = 1.2$, and $b = 1830$.

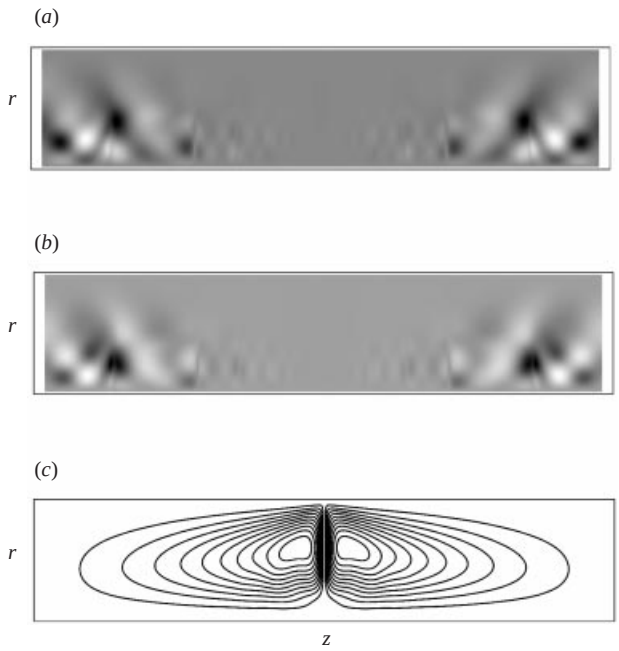

FIGURE 18. Density plot of v_r showing (*a*) the real and (*b*) the imaginary parts of the destabilizing disturbance, and (*c*) the streamlines of the base diwhirl. Note that the core of the diwhirl is entirely unaffected by the disturbance. The parameters are $We_\theta = 23.87$, $S = 1.2$, $\epsilon = 0.20$, $b = 1830$, and $L = 4.74$.

distinct from the oscillatory finite-wavelength axisymmetric pattern arising from the linear instability of circular Couette flow.

For non-axisymmetric disturbances, the stability picture is somewhat more complicated. We performed computations with $n = 1$ and $n = 2$ and found three pairs of unstable complex conjugate eigenvalues. Their growth rates are summarized in table 1, while their structures are shown in figures 19 and 20. For $n = 1$, we see that there are two modes that have their largest amplitude close to the core of the diwhirl (figures 19*a* and 19*b*), while the third (figure 19*c*) has a large amplitude away from the core. The third mode is directly related to the linear instability of circular Couette flow with respect to non-axisymmetric disturbances with $n = 1$. For $n = 2$, the picture is slightly different. There is still one mode (figure 19*a*) that is largely concentrated outside the core, and which therefore seems related to the linear instability of circular Couette flow. The mode in figure 19(*b*) is largely concentrated at the core, and shows similarities to figures 19(*a*) and 19(*b*). In addition, there is a non-localized mode (figure 20*c*) that is absent for $n = 1$. As discussed in § 4.3, we expect that with increasing

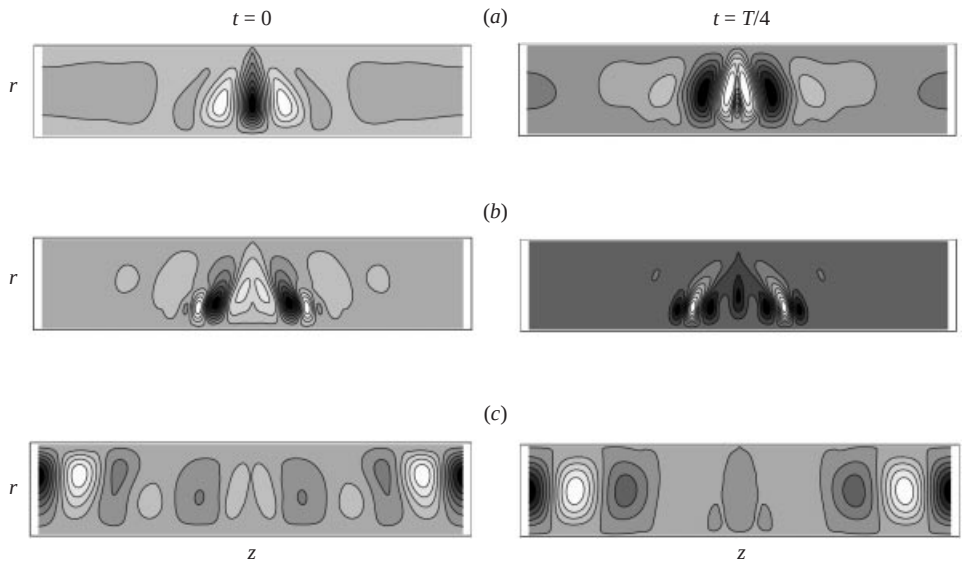

FIGURE 19. Density plot of the perturbation radial velocity for the three non-axisymmetric unstable eigenmodes with $n = 1$. The parameters are identical to those in figure 18.

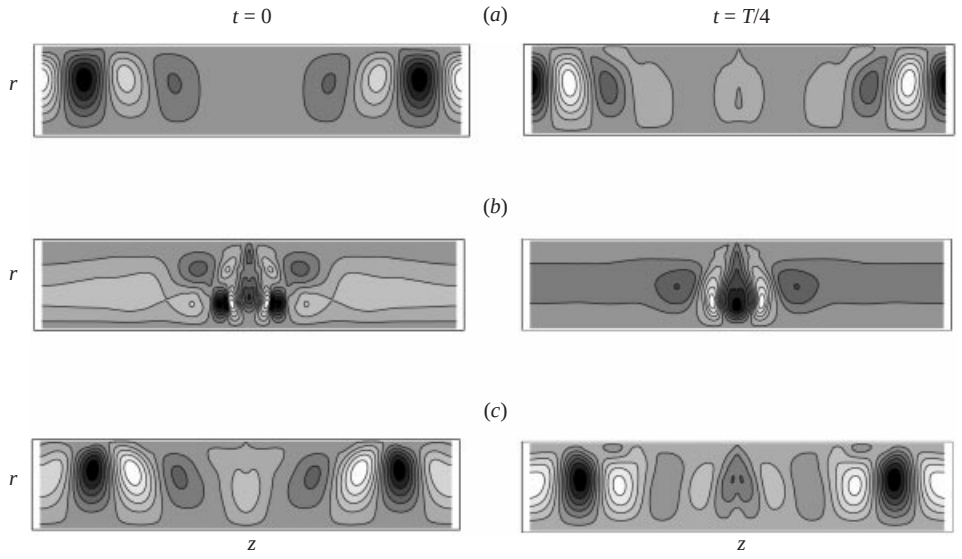

FIGURE 20. Density plot of the perturbation radial velocity for the three non-axisymmetric unstable eigenmodes with $n = 2$. The parameters are identical to those in figure 18.

b, the diwhirls would come into existence below the linear stability limit of circular Couette flow. In these regimes, they would be stable, at least with respect to the 'far field' linear instabilities that do not affect the core of the diwhirl.

4.6. *Dean flow revisited*

In the previous sections, we have demonstrated that stationary, localized solutions of arbitrarily large wavelength exist in circular Couette flow. Here, we return to Dean flow to investigate whether such solitary solutions are possible there. We do this by

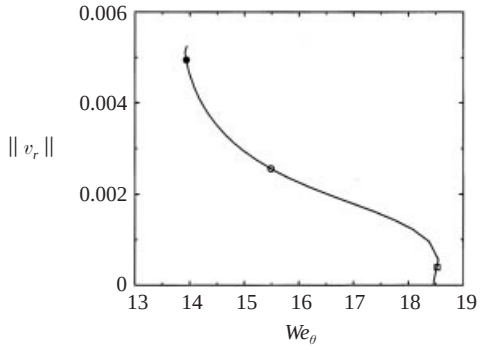

FIGURE 21. Bifurcation diagram for Dean flow at $b = 1830$, $S = 1.2$, $\epsilon = 0.2$, and $L = 1.963$. We could not continue the branch beyond $We_\theta = 13.94$, for reasons discussed in section 4.6. Radial velocity profiles corresponding to the points marked by the open square and filled and open circles are shown in figure 22.

tracking long-wavelength steady states that bifurcate from the base state in Dean flow. To make comparison with the circular Couette flow results easier, we choose $b = 1830$, $S = 1.2$, and $\epsilon = 0.2$, which are the same parameter values that we used for circular Couette flow. In figure 21, we show the bifurcation diagram for $L = 1.963$. This is similar to figure 5, in that there is a large subcritical region, and the non-trivial branch exhibits a turning point, i.e. there is a critical value of the Weissenberg number below which the non-trivial solution does not exist. In figure 22, we show density plots of $\alpha_{\theta\theta}$ at $We_\theta = 18.525$ (marked by an open square in figure 21), $We_\theta = 15.486$ (marked by an open circle in figure 21) and at $We_\theta = 13.930$ (marked by a filled circle in figure 21). The figure shows that rather than becoming localized, as would have been the case with the diwhirls in circular Couette flow, long-wavelength nonlinear patterns in Dean flow have a tendency to split into two vortices, each one having half the wavelength of the original vortex. In fact, for the particular case of $L = 1.963$, we were not able to advance the continuation beyond $We_\theta = 13.94$ on the upper branch. Examination of figure 22(c) reveals why: it is clear from the symmetry of the solution that the $L = 1.963$ path crosses a branch of solutions with $L = 1.963/2$ in a pitchfork bifurcation. This intersection is the reason the continuation fails beyond this point. We wish to stress here that the absence of localization in Dean flow is not limited to the particular case of $L = 1.963$: we have seen this for larger values of L as well. One possible reason for this could be that localized structures would have areas in the far field that would be very similar to base-state Dean flow, much like the case with solitary steady states in circular Couette flow where the far field is essentially base-state circular Couette flow (see figure 8). However, since Dean flow is linearly unstable to stationary disturbances of smaller wavelengths, there would be a tendency for stationary vortex structures of smaller wavelengths to form in the far field and prevent true localization.

As with circular Couette flow in figure 10, we can plot an existence boundary for the non-trivial Dean flow solutions. This curve is shown in figure 23. Note that there is a discontinuity at $L = 1.795$. At this wavelength, we get a collision with the $L = 1.795/2$ branch in a pitchfork bifurcation as was the case with $L = 1.963$, but this time, the collision occurs before the turning point is reached. Therefore, no turning point exists for this value of L, resulting in the discontinuity. For reference, we also show two linear stability curves of Dean flow. The curve on the left (the dashed

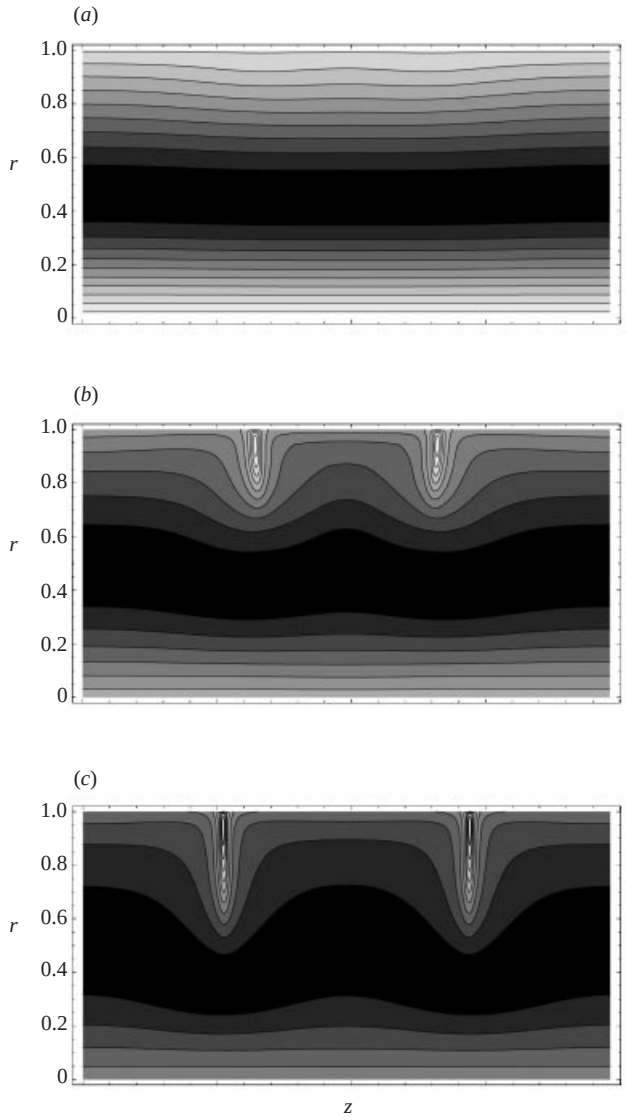

FIGURE 22. Density plots of $\alpha_{\theta\theta}$ at the points marked in figure 21. (*a*) $We_\theta = 18.525$, (*b*) $We_\theta = 15.486$, (*c*) $We_\theta = 13.930$.

line) is the usual linear stability curve of $We_{\theta,c}$ versus L. The curve on the right (the dotted line) is the linear stability curve with respect to disturbances which have two vortices, each of wavelength $L/2$. This curve is trivially obtained from the regular linear stability diagram by multiplying the horizontal coordinate by a factor of two. At the intersection of the two curves, denoted by L_t, is a codimension-2 point, where disturbances of wavelength L_t and $L_t/2$ bifurcate simultaneously. We would expect interactions between modes to play a significant role in the nonlinear behaviour close to this wavelength. Note that the discontinuity in the nonlinear existence curve occurs close to $L = L_t$. In short, while localized states are supported in viscoelastic circular Couette flow, in Dean flow they are not.

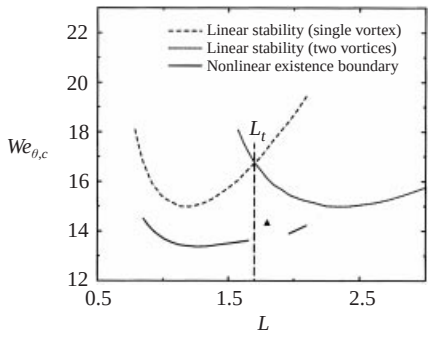

FIGURE 23. Linear stability curves and existence boundaries for nonlinear solutions in Dean flow at $S = 1.2$, $\epsilon = 0.2$, and $b = 1830$. The filled triangle shows the result at $L = 1.795$, where the solution terminates via collision with the $L/2$ branch in a pitchfork bifurcation, without having gone through a turning point.

5. Conclusions

In this work, we have computed stationary, non-trivial solutions in viscoelastic circular Couette and Couette–Dean flows. These stationary solutions, computed with the FENE-P constitutive model, show very strong spatial localization, exist only for large values of the polymer extensibility parameter and large wavelengths, show a hysteretic character in the Weissenberg number, and are isolated from the base Couette flow branch of solutions, all of which are characteristics shared by similar patterns ('diwhirls' or 'flame patterns') observed experimentally (Groisman & Steinberg 1997, 1998; Baumert & Muller 1999). Direct comparison shows that the streamlines and magnitudes of the radial velocity for the patterns we have computed are very similar to the corresponding experimentally measured quantities. The one major difference between the experimenatally observed patterns and our solutions is the position of the turning point bifurcation at which the diwhirls come into existence. While the experimentally observed diwhirls exist at Weissenberg numbers well below the linear stability limit of circular Couette flow, the computed diwhirls come into existence at Weissenberg numbers slightly higher than the linear stability limit of the base state. A likely reason for this discrepancy is our present inability to computationally access large enough values of b.

We have also performed computations with the FENE-CR model, finding that it produces significantly different results in both the linear and nonlinear regimes. In particular, the diwhirls are not predicted with the FENE-CR model for the parameter values that we have examined. However, since both the FENE-P and FENE-CR models collapse to the Oldroyd-B model as $b \to \infty$, we would expect the FENE-CR model to exhibit diwhirls at sufficiently large values of b.

We have used the velocity and stress fields generated from our computations to propose a self-sustaining mechanism for the diwhirls. The mechanism arises from a finite-amplitude perturbation giving rise to a local increase in the azimuthal velocity near the outer cylinder near the symmetry axis of the vortices. This gives rise to an unstable stratification of stress, which drives inward radial motion. As the fluid moves inward, it is accelerated azimuthally by the base-state shear generated by the motion of the inner cylinder. The tension in the streamlines then pulls fluid close to the outer cylinder axially into the diwhirl core, then forward and down, regenerating the unstable stress stratification and resulting in a self-sustaining mechanism.

Linear stability analysis shows that the computed diwhirls are unstable with respect

to axisymmetric and non-axisymmetric perturbations. For axisymmetric disturbances, the destabilizing disturbance has appreciable amplitude only in the region away from the diwhirl core, and is therefore linked to the linear instability of the base state in the Weissenberg number regimes in which the diwhirls we have computed exist. The picture is more complicated for non-axisymmetric disturbances, with some unstable eigenvectors only having appreciable amplitude away from the core and others being concentrated at the core of the diwhirl.

Finally, we have investigated whether structures similar to diwhirls or flame patterns could form in Dean flow by tracking steady states bifurcating from the base flow in Weissenberg number. Our computations demonstrate that long-wavelength solutions in Dean flow tend to evolve into shorter-wavelength structures rather than becoming localized.

Along with the solutions arising from the linear instability of the circular Couette flow base state, we propose that the solitary solutions we have computed form building blocks for spatiotemporal dynamics in the flow of viscoelastic liquids. We believe that the computations presented here are a step towards understanding these complex nonlinear dynamics.

We gratefully acknowledge financial support for this work from NSF, the ACS/PRF and 3M Company. The bulk of the computations presented here were performed on one or more four processor SGI Origin 200 machines, and we thank the Chemical Engineering Department at the University of Wisconsin-Madison for providing us with access to these machines. We would also like to thank Professor Bamin Khomami, Professor R. Sureshkumar and their research associates for helpful discussions.

REFERENCES

Al-Mubayedh, U. A., Sureshkumar, R. & Khomami, B. 1999 Influence of energetics on the stability of viscoelastic Taylor-Couette flow. *Phys. Fluids* **11**, 3217–3226.

Baumert, B. M. & Muller, S. J. 1995 Flow visualization of the elastic Taylor-Couette instability in Boger fluids. *Rheol. Acta* **34**, 147–159.

Baumert, B. M. & Muller, S. J. 1997 Flow regimes in model viscoelastic fluids in a circular Couette system with independently rotating cylinders. *Phys. Fluids* **9**, 566–586.

Baumert, B. M. & Muller, S. J. 1999 Axisymmetric and non-axisymmetric elastic and inertio-elastic instabilities in Taylor-Couette flow. *J. Non-Newtonian Fluid Mech.* **83**, 33–69.

Beavers, G. S. & Joseph, D. D. 1974 Tall Taylor cells in polyacrylamide solutions. *Phys. Fluids* **17**, 650–651.

Bird, R. B., Armstrong, R. C. & Hassager, O. 1987*a* *Dynamics of Polymeric Liquids*, 2nd edn., vol. 1. Wiley.

Bird, R. B., Curtiss, C. F., Armstrong, R. C. & Hassager, O. 1987*b* *Dynamics of Polymeric Liquids*, 2nd edn., vol. 2. Wiley.

Brooks, A. N. & Hughes, T. J. R. 1982 Streamline upwind/Petrov-Galerkin formulations for convection dominated flows with particular emphasis on the incompressible Navier-Stokes equations. *Comp. Methods Appl. Mech. Engng* **32**, 199–259.

Cherhabili, A. & Ehrenstein, U. 1995 Spatially localized two-dimensional finite amplitude states in plane Couette flow. *Eur. J. Mech.* B/*Fluids* **14**, 677–696.

Cherhabili, A. & Ehrenstein, U. 1997 Finite-amplitude equilibrium states in plane Couette flow. *J. Fluid Mech.* **342**, 159–177.

Chilcott, M. D. & Rallison, J. M. 1988 Creeping flow of dilute polymer solutions past cylinders and spheres. *J. Non-Newtonian Fluid Mech.* **29**, 381–432.

Christodoulou, K. N. & Scriven, L. E. 1988 Finding leading modes of a viscous free surface flow: An asymmetric generalized eigenproblem. *J. Sci. Comput.* **3**, 355–406.

Cross, M. C. & Hohenberg, P. 1993 Pattern-formation outside of equilibrium. *Rev. Mod. Phys.* **65**, 851–1112.

Fineberg, J. & Lioubashevski, O. 1998 Propagating solitary states in highly dissipative driven fluids. *Physica* A **249**, 10–17.

Graham, M. D. 1998 Effect of axial flow on viscoelastic Taylor-Couette instability. *J. Fluid Mech.* **360**, 341–374.

Grillet, A. M., Lee, A. G. & Shaqfeh, E. S. G. 1999 Observations of ribbing instabilities in elastic fluid flows with gravity stabilization. *J. Fluid Mech.* **399**, 49–83.

Groisman, A. & Steinberg, V. 1997 Solitary vortex pairs in viscoelastic Couette flow. *Phys. Rev. Lett.* **78**, 1460–1463.

Groisman, A. & Steinberg, V. 1998 Mechanism of elastic instability in Couette flow of polymer solutions: Experiment. *Phys. Fluids* **10**, 2451–2463.

Groisman, A. & Steinberg, V. 2000 Elastic turbulence in a polymer solution flow. *Nature* **405**, 53–55.

Heinrichs, R., Ahlers, G. & Cannell, D. S. 1987 Traveling waves and spatial variation in the convection of a binary mixture. *Phys. Rev.* A **35**, 2761–2764.

Herrchen, M. & Öttinger, H. C. 1997 A detailed comparison of various FENE dumbbell models. *J. Non-Newtonian Fluid Mech.* **68**, 17–42.

Joo, Y. L. & Shaqfeh, E. S. G. 1992 A purely elastic instability in Dean and Taylor-Dean flow. *Phys. Fluids* A **4**, 524–543.

Joo, Y. L. & Shaqfeh, E. S. G. 1994 Observations of purely elastic instabilities in the Taylor-Dean flow of a Boger fluid. *J. Fluid Mech.* **262**, 27–73.

Khayat, R. E. 1999 Finite-amplitude Taylor-vortex flow of viscoelastic liquids. *J. Fluid. Mech* **400**, 33–58.

Kolodner, P., Bensimon, D. & Surko, C. M. 1988 Traveling-wave convection in an annulus. *Phys. Rev. Lett.* **60**, 1723–1726.

Lange, M. & Eckhardt, B. 2001 Diwhirls in viscoelastic Couette-Taylor flow. *Phys. Rev.* E (in press).

Larson, R. G., Shaqfeh, E. S. G. & Muller, S. J. 1990 A purely elastic instability in Taylor-Couette flow. *J. Fluid Mech.* **218**, 573–600.

Lehoucq, R. B., Sorensen, D. C. & Yang, C. 1997 *Arpack Users Guide: Solution of Large Scale Eigenvalue Problems by Implicitly Restarted Arnoldi Methods.* `ftp://ftp.caam.rice.edu/pub/software/ARPACK`.

Lioubashevski, O., Arbell, H. & Fineberg, J. 1996 Dissipative solitary states in driven surface waves. *Phys. Rev. Lett.* **76**, 3959–3962.

Lioubashevski, O., Hamiel, Y., Agnon, A., Reches, Z. & Fineberg, J. 1999 Oscillons and propagating solitary waves in a vertically vibrated colloidal suspension. *Phys. Rev. Lett.* **83**, 3190–3193.

McKinley, G. H., Pakdel, P. & Öztekin, A. 1996 Rheological and geometric scaling of purely elastic instabilities. *J. Non-Newtonian Fluid Mech.* **67**, 19–47.

Marchal, J. M. & Crochet, M. J. 1987 A new mixed finite-element for calculating viscoelastic flow. *J. Non-Newtonian Fluid Mech.* **26**, 77–114.

Moses, E., Fineberg, J. & Steinberg, V. 1987 Multistability and confined traveling-wave patterns in a convecting binary mixture. *Phys. Rev.* A **35**, 2757–2760.

Patera, A. T. 1984 A spectral element method for fluid dynamics: Laminar flow in a channel expansion. *J. Comput. Phys.* **54**, 468–488.

Ramanan, V. V., Kumar, K. A. & Graham, M. D. 1999 Stability of viscoelastic shear flows subjected to steady or oscillatory transverse flow. *J. Fluid Mech.* **379**, 255–277.

Renardy, M. 2000 Location of the continuous spectrum in complex flows of the UCM fluid. *J. Non-Newtonian Fluid Mech.* **94**, 75–85.

Renardy, Y., Renardy, M., Sureshkumar, R. & Beris, A. N. 1996 Hopf-Hopf and steady-Hopf mode interactions in Taylor-Couette flow of an upper convected Maxwell liquid. *J. Non-Newtonian Fluid Mech.* **63**, 1–31.

Saad, Y. 1996 *Iterative Methods for Sparse Linear Systems.* PWS.

Saad, Y. & Schultz, M. H. 1986 GMRES: A generalized minimal residual algorithm for solving nonsymmetric linear systems. *SIAM J. Sci. Statist. Comput.* **7**, 856–869.

Seydel, R. 1994 *Practical Bifurcation and Stability Analysis.* Springer.

Shaqfeh, E. S. G. 1996 Purely elastic instabilities in viscometric flows. *Ann. Rev. Fluid Mech.* **28**, 129–185.

Sureshkumar, R., Beris, A. N. & Avgousti, M. 1994 Non-axisymmetric subcritical bifurcations in viscoelastic Taylor-Couette flow. *Proc. R. Soc. Lond.* A **447**, 135–153.

Umbanhowar, P., Melo, F. & Swinney, H. L. 1996 Localized excitations in a vertically vibrated granular layer. *Nature* **382**, 793–796.

Wilson, H. J., Renardy, M. & Renardy, Y. 1999 Structure of the spectrum in zero Reynolds number shear flow of the UCM and Oldroyd-B liquids. *J. Non-Newtonian Fluid Mech.* **80**, 251–268.

Wu, J., Keolian, R. & Rudnick, I. 1984 Observation of a nonpropagating hydrodynamic soliton. *Phys. Rev. Lett.* **52**, 1421–1424.

Wu, J., Wheatley, J., Putterman, S. & Rudnick, I. 1987 Observation of envelope solitons in solids. *Phys. Rev. Lett.* **59**, 2744–2747.